Editors' Suggestion

Magnetoelectric imprint of skyrmions in van der Waals bilayers

Zhong Shen, Xiaoyan Yao,* and Shuai Dong†

Key Laboratory of Quantum Materials and Devices of Ministry of Education, School of Physics, Southeast University, Nanjing 211189, China

(Received 12 July 2024; revised 29 September 2024; accepted 6 March 2025; published 17 March 2025)

As topological solitons in real space, magnetic (M)/electric (E) skyrmions have attracted enduring attention due to their significant roles in both fundamental science and potential information-related applications. However, it remains challenging to effectively track/manipulate M skyrmions via energy-saving routes. Besides, the stability of E skyrmions usually require harsher conditions than their M counterparts. Here, a strategy so-called magnetoelectric imprint is proposed to overcome these obstacles. Through proximate interactions, an isoperiodic bijection is established between the local dipoles and spin moments. Thus, M skyrmions can be mapped into E skyrmions, which provides an alternative strategy to detect/manipulate M skyrmions by recognizing/controlling their E fingerprints. More interestingly, these magnetism induced E skyrmions come from the distortions of electron clouds instead of lattice, which provides an inborn superior for ultra-high-speed dynamics. Our work goes beyond the conventional separating territories of M/E skyrmions by demonstrating an emerging quasiparticle, i.e., the ME skyrmions, thus opens one more route to realize magnetoelectric functions in low-dimensional materials.

DOI: 10.1103/PhysRevB.111.104422

I. INTRODUCTION

Magnetic (M) skyrmions are vortexlike spin textures with integral topological numbers, which open a promising direction for spintronics [1,2]. Since the experimental observations of M skyrmions in reciprocal space [3] and real space [4], the physical mechanisms of their creation and manipulation have been extensively studied, and more and more materials with M skyrmions have been predicted/found [5–11]. Up to now, M skyrmions can be directly visualized by Lorentz transmission electron microscopy [4] and spin-polarized scanning tunneling microscopy [12,13], which sets a high technical threshold for experimental direct characterizations. Thus, other easier experimental routes are urgently needed to track and manipulate M skyrmions directly. Although the electrical readout of M skyrmions was attempted, such as spin-mixing magnetoresistance (XMR) [14,15] and chiral XMR (C-XMR) [16] based on current signals, and the dielectric/ferroelectric responses of M skyrmion based on electric field signals. The Joule heat is inevitable in magnetoresistance measurements while the dielectric/ferroelectric responses only works in insulators [17–21].

The electric (E) skyrmions, with similar topological textures of electric dipoles, were also proposed and experimentally realized in $PbTiO_3/SrTiO_3$ superlattices [22]. Later, the concept of E skyrmions/vortex has been generalized to more systems [23–28]. Novel physics, e.g., large second harmonic generation (SHG), negative capacitance, and emergent chirality, have been reported for E skyrmions [25,29,30]. Different from the M skyrmions, the E skyrmions can be directly regulated by electric field, which is much easier and more energy-efficient. However, current E skyrmions are mostly limited in titanates and their superlattices [23–27]. Usually, the complex interplay among elastic, electrostatic, and gradient energy is required to stabilize the E skyrmions [31], namely the origin of E skyrmions is mostly related to the electric-mechanical coupling. It is as expected since in these systems the electric dipoles are from structural distortions.

In some new kinds of ferroelectrics, the distortion of electron clouds can also contribute a lot to the local dipoles and macroscopic polarizations. For example, in the type-II multiferroic o-$HoMnO_3$ and $Hf_2VC_2F_2$, the magnetism-induced polarizations can be mostly from the distortion of electron clouds, instead of the structural distortions [32,33]. Another case is the sliding ferroelectrics in van der Waals (vdW) materials [34,35], in which the polarization originates from the bias of electron clouds due to the interlayer interaction [36]. Comparing with those conventional dipoles from structural distortions, these electronic-originated dipoles are naturally advantageous for ultra-high-speed switching since the dynamics of electrons are much faster than ions. Thus, it will be highly interesting and vital to pursue E skyrmions with dipoles from electron clouds distortion.

In this paper, we propose a mechanism to generate E skyrmions by rubbing M skyrmions to adjacent ferromagnetic layer, which is coined as magnetoelectric imprint (MEI). Microscopically, the dipoles come from the electron clouds distortion, which is spin-orientation dependent. Based on this MEI effect, M skyrmions can be read/manipulated using pure electrical field methods. Our work is mainly based on first-principles density of functional theory (DFT) calculations and atomistic simulation of the spin lattice model, and more details can be found in the Methods section.

*Contact author: yaoxiaoyan@seu.edu.cn
†Contact author: sdong@seu.edu.cn

II. METHODS

A. First-principles calculations

The first-principles density functional theory (DFT) calculations are performed using the Vienna *ab initio* simulation package (VASP) [37]. The generalized gradient approximation (GGA) of Perdew-Burke-Ernzerhof (PBE) is used for the exchange-correlation functional [38]. The energy cutoff for plane-wave basis is set as 500 eV. The lattice constants and ionic positions are fully optimized with high convergent criteria for energy (10^{-8} eV) and the Hellman-Feynman forces (10^{-3} eV/Å). The first Brillouin-zone integration is carried out by using a $9 \times 9 \times 1$ Γ-centered k-point mesh. For the calculation of single-ion magnetocrystalline anisotropy, a more intensive k-point mesh of $17 \times 17 \times 1$ is used with the convergent criteria for energy being 10^{-6} eV. To consider the on-site Coulomb interaction of Cr's $3d$ electrons, an effective Hubbard term U_{eff} of 1.5 eV is applied [39,40]. A vacuum spacing more than 20 Å is adopted along the z axis to avoid the interaction between two neighboring slices.

To confirm the dynamic stability of CrTeI bilayer, the phonon band structures are calculated by using the PHONOPY code [41,42], with a $4 \times 4 \times 1$ supercell. The ferroelectric polarization is calculated using the Berry phase method [43,44]. The visualization of crystal structures and differential electron density are realized by VESTA [45].

B. Model simulation

The atomistic simulations are carried out based on the spin lattice model, which is solved via the Landau-Lifshitz-Gilbert (LLG) equation [46,47] as implemented in the SPIRIT package [48]. The Hamiltonian can be expressed as

$$H = J_1 \sum_{\langle i,j \rangle} \mathbf{S}_i \cdot \mathbf{S}_j + J_2 \sum_{\langle i,k \rangle} \mathbf{S}_i \cdot \mathbf{S}_k + J_3 \sum_{\langle i,l \rangle} \mathbf{S}_i \cdot \mathbf{S}_l + \sum_{\langle i,j \rangle} \mathbf{D}_{ij} \cdot (\mathbf{S}_i \times \mathbf{S}_j) + K \sum_i \left(S_i^z\right)^2.$$

Here, $\mathbf{S}_{i,j,k,l}$ is the normalized spin at site i, j, k, l. $J_1/J_2/J_3$ are the first/second/third-nearest-neighbor Heisenberg-type exchange. The magnetic anisotropy and Dzyaloshinskii-Moriya interaction are characterized by K and $\mathbf{D}_{ij}$. The dipole-dipole interaction is not included because it doesn't play any dominant role for the simulation results, as shown in Fig. S15 in the Supplemental Material (SM) [49]. In these simulations, a large supercell containing 23 200 magnetic sites is adopted with periodic boundary conditions, and bilayer Cr sublattice is used with the initial spin configuration being a random state.

III. RESULTS AND DISCUSSION

A. Sliding magnetic bilayers

Our model system is CrTeI bilayer, as shown in Fig. 1(a). In each monolayer, the magnetic Cr cation is sandwiched by two sheets of nonmagnetic anions (I and Te), forming a hexagonal lattice with a point group C_{3v}. We chose CrTeI for the following reasons. First, the Janus monolayer naturally breaks the spatial inversion symmetry along the off-plane direction, which provides an inborn Dzyaloshinskii-Moriya interaction

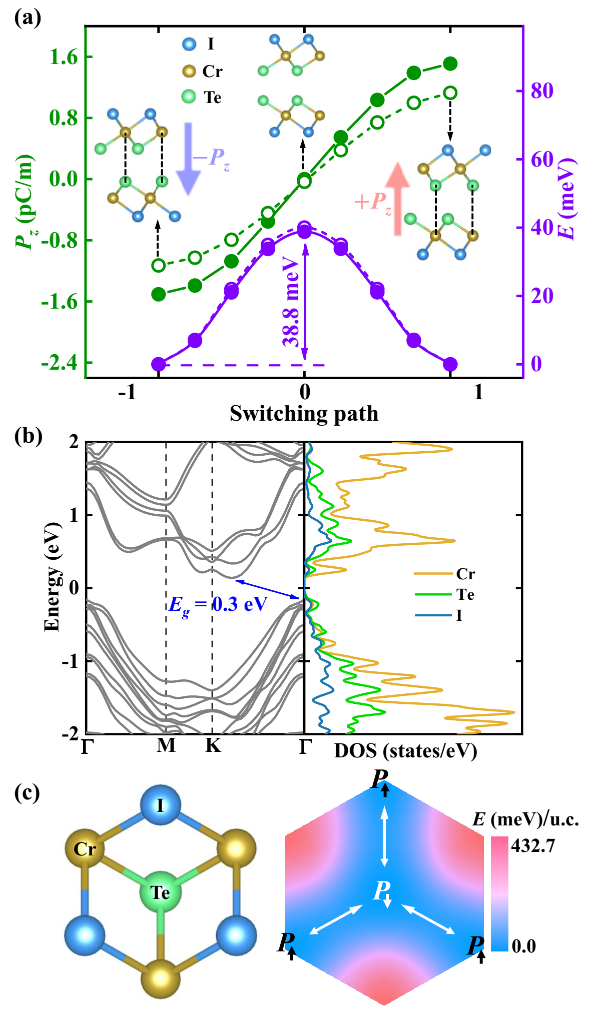

FIG. 1. Physical properties of CrTeI bilayer. (a) The off-plane ferroelectric polarization (green dots) and switching energy barrier (purple dots) along possible switching path, with A-type antiferromagnetic order. Open symbols: the polarization and barrier obtained with ferromagnetic order. Insets: the side views of ferroelectric and paraelectric states. (b) Electronic structure. Left: band structure; Right: element-projected density of states (DOS). (c) Left: the top view of CrTeI. Right: the energy map for sliding.

(DMI), a key driving force for M skyrmions [50,51]. Second, the heavy elements (Te and I) are advantageous to obtain strong spin-orbit coupling (SOC), guaranteeing a large DMI in this Janus monolayer. Last, for practical consideration, similar Janus structure, e.g., MoSSe [52,53], has been synthesized experimentally.

Considering the asymmetric upper/lower surfaces of Janus structure, there are at least three kinds of stacking sequences for CrTeI bilayer: (i) Te-I—Te-I, (ii) Te-I—I-Te, and (iii) I-Te—Te-I. As compared in Fig. S1 in the SM [49], the I-Te—Te-I stacking sequence owns the lowest energy, which will be studied in the following. Then the most stable structures, i.e., the $\pm P_z$ states in Fig. 1(a), are obtained by relaxing the structure from different initial structures (Fig. S2 in the SM [49]). And the dynamic stability of the $\pm P_z$ structures is confirmed by the phonon dispersion spectrum [Fig. S2(m) in the SM [49]].

As demonstrated in Fig. S3 in the SM [49], the interlayer magnetic coupling is found to be antiferromagnetic, while the intralayer coupling is ferromagnetic. Thus, the ground state is the A-type antiferromagnetism. The magnetocrystalline anisotropy is also calculated, which supports a magnetic easy axis along the off-plane direction.

Then the electronic structure is calculated based on the GGA+U method ($U_{\text{eff}} = 1.5$ eV for Cr's $3d$ orbitals) with SOC, for the A-type antiferromagnetic state. An indirect band gap is obtained, as shown in Fig. 1(b). It is well known that DFT systematically underestimates band gaps. Additionally, the Heyd-Scuseria-Ernzerhof (HSE06) hybrid functional [54,55] was also tested, which leads to a larger band gap 0.8 eV [Fig. S3(d) in the SM] [49].

Although the I-Te—Te-I stacking sequence seems to be centrosymmetric, off-plane polarizations ($\pm P_z$) can emerge from the interlayer sliding, i.e., the sliding ferroelectricity. As shown in Fig. 1(a), the bistable $+P_z$ and $-P_z$ states can be switched via sliding. The amplitude of P_z reaches 1.51 pC/m, which is almost an order of magnitude larger than that of T_d-WTe_2 (0.2 pC/m) [56,57], and comparable to those of heterobilayer MoS_2/WS_2 (1.45 pC/m) [58] and bilayer h-BN (1.88 pC/m) [59,60]. This sliding-dependent P_z is mostly SOC independent. And the switching barrier is moderate 38.8 meV/u.c., close to the case of ZrI_2 [36]. According to the energy landscape [Fig. 1(c)], this interlayer sliding direction is along the projection direction of I-Te bonds.

The above results are obtained with the A-type antiferromagnetic condition. By using the ferromagnetic conditions, the above conclusion of sliding ferroelectricity and its switching barrier remain robust, although the amplitude of polarization will be changed accordingly [open symbols in Fig. 1(a)]. In other words, the interlayer magnetic order can quantitatively tune the sliding ferroelectric polarization in CrTeI bilayer, implying a direct magnetoelectricity. Similar behavior was also found in $CrI_3/MnSe_2$ vdW heterostructure [61].

B. Magnetoelectric imprint

Above direct magnetoelectricity is based on collinear magnetic orders, which can be extended to more general cases, i.e., interlayer noncollinear configurations. To study this effect, all spins in the bottom layer are fixed ferromagnetically along the off-plane $+z$ direction if not noted explicitly, denoted as the frozen layer. Then the orientation of spins in the top layer is rotated as a whole (denoted as the free layer), characterized by its polar angle θ and azimuthal angle φ.

First, by keeping $\theta = 90^\circ$ in the free layer, the evolution of polarization is calculated as a function of φ. As shown in Fig. 2(a), the z component of polarization (P_z) is almost a constant, while the in-plane components (P_x and P_y) change significantly and periodically, namely the vector $\mathbf{P}_{xy}$ synchronously rotates following the spins in the free layer, i.e., $\mathbf{P}_{xy}||\mathbf{S}_{xy}$. Coincidentally, the amplitudes of spin-induced P_{xy} and the sliding-induced P_z are almost identical: ~1.4 pC/m. Thus, the vector of total ferroelectric polarization $\mathbf{P}$ forms a conical trajectory with solid angle ~45°.

Second, this spin-dependent $\mathbf{P}_{xy}$ originates from SOC, which is zero without SOC [open symbols in Fig. 2(a)]. If

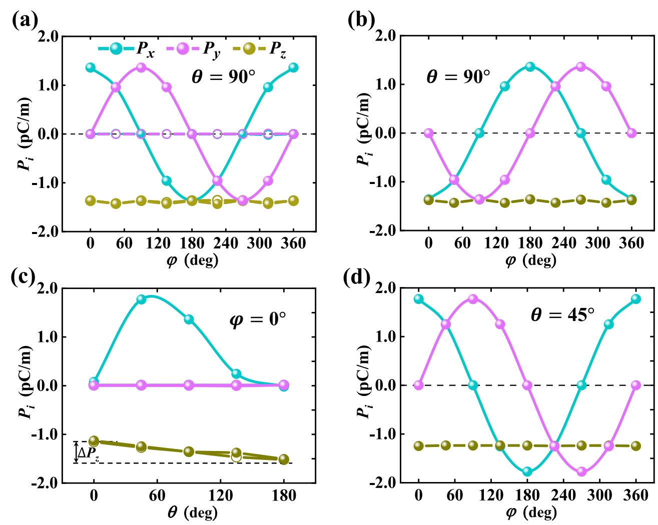

FIG. 2. Spin-dependent polarization (P_x, P_y, P_z) in CrTeI bilayer. Here θ and φ are the polar and azimuthal angles of the free-layer spins $\mathbf{S}$, while the frozen-layer spins are fixed along $+z$ [or $-z$ in (b)]. (a) $\theta = 90^\circ$. The evolution of (P_x, P_y) follows (S_x, S_y) synchronously. For comparison, (P_x, P_y) disappears when SOC is switched off (open symbols). (b) The same as (a) but the frozen-layer spins are fixed along $-z$. (c) $\varphi = 0^\circ$. (d) $\theta = 45^\circ$.

the spins in the frozen layer are fixed to $-z$, the induced $\mathbf{P}_{xy}$ becomes antiparallel to the spins' orientation in the free layer, i.e., $-\mathbf{P}_{xy}||\mathbf{S}_{xy}$, as shown in Fig. 2(b).

Third, the polar angle θ is tuned with fixed $\varphi = 0^\circ$, which leads to a moderate change of P_z ($\Delta P_z \approx 0.4$ pC/m ~$1/3P_z$). Meanwhile, P_x changes significantly within one period and P_y is zero, as shown in Fig. 2(c). Noting that $P_x(\theta)$ is asymmetric with respect to $\theta = 90^\circ$, due to the broken mirror symmetry caused by interlayer sliding and the spins of the frozen layer. Further, ΔP_z becomes opposite once the fixed spins in the bottom layer is reversed to $-z$ (not shown here). Different from $\mathbf{P}_{xy}$, ΔP_z is not SOC originated [see open symbols in Fig. 2(c) for the non-SOC results]. For completeness, more evolutions of θ-dependent $\mathbf{P}$ for other fixed φ's are shown in Fig. S4 in the SM [49].

Fourth, the φ-dependent $P_x/P_y/P_z$ component for $\theta = 45^\circ$ are shown in Fig. 2(d), which is qualitatively identical to the $\theta = 90^\circ$ case.

According to aforementioned results, the vector $\mathbf{P}$ can be phenomenologically expressed as

$$\mathbf{P} = P_0\hat{z} + (\mathbf{S}_f \cdot \hat{z})(aS_x\hat{x} + aS_y\hat{y} + bS_z\hat{z}), \qquad (1)$$

where $\mathbf{S}$ ($\mathbf{S}_f$) is the normalized spin vector of the free (frozen) layer and P_0 is the base line of sliding polarization. The signs of coefficients a/b are determined by the frozen layer spins, as an indication of interlayer coupling and requested by the time-reversal symmetry of $\mathbf{P}$. Most importantly, there is a bijection between $\mathbf{P}$ and $\mathbf{S}$, i.e., one-to-one correspondence, coined as the MEI here. In the microscopic level, such bijection relies on the hybrid mechanisms of exchange strictions [62] and the KNB model [63] (Fig. S5 in the SM [49]).

Then it is interesting to ask whether the MEI function can persist when there is no sliding between CrTeI bilayers. As

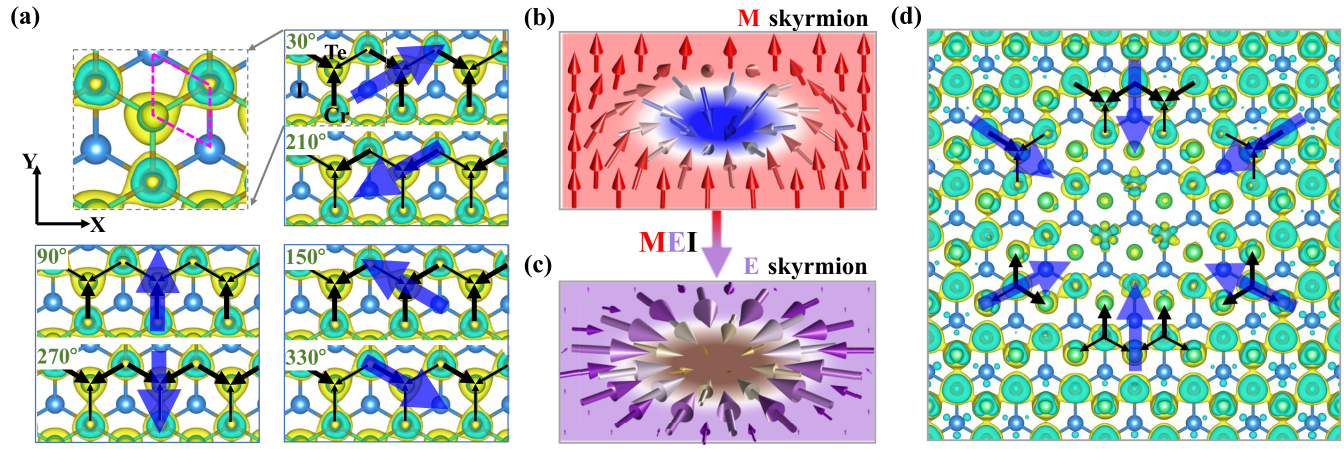

FIG. 3. Visualization of magnetoelectric imprint. (a) Image of differential electron density (DED) of the frozen layer as a function of uniform spin orientation of the free layer. Here $\theta = 90^\circ$ without loss of generality. The DED is defined as $\delta\rho(\mathbf{r}) = \rho_S(\mathbf{r}) - \rho_0(\mathbf{r})$, where $\rho_S(\mathbf{r})$ is the electron density at position $\mathbf{r}$ for giving $\mathbf{S}$ of the top layer and $\rho_0(\mathbf{r})$ is the ground state one. Black arrows: Local dipoles of Cr-Te bonds defined as $\mathbf{d} = -e\int_V \delta\rho(\mathbf{r})d\mathbf{r}$, where e is the elementary charge and V is the volume of each bond (pink rhombus). Blue arrows: the net polarization. (b) The M skyrmion in the free layer used in DFT calculation. (c) The E skyrmion generated in the frozen layer, derived via the bijection relation. (d) The corresponding DED of the frozen layer obtained from DFT, which shows the evidence of an E skyrmion.

shown in Fig. S6 in the SM [49], for the nonpolar stacking bilayer (space group $P\bar{6}m2$), the in-plane component $\mathbf{P}_{xy}$ can still follow $\mathbf{S}$ of the top layer, with reduced amplitude ($\sim$50% of $\mathbf{P}_{xy}$). However, the P_z component becomes negligible, despite the orientation of $\mathbf{S}$. In other words, the breaking reversal symmetry along the z axis is a precondition to the full MEI function.

The magnetism induced $\mathbf{P}$ can be visualized using the differential electron density (DED) of the frozen layer. As shown in Fig. 3(a), the three Cr-Te bonds are no longer equivalent when $\mathbf{S}_{xy}$ is nonzero, breaking the in-plane C_3 rotational symmetry (See Fig. S7 for more details). Then a local electric dipole can be generated for each bond. These bond dipoles are shown as black arrows in Fig. 3(a) and the macroscopic $\mathbf{P}_{xy}$ (blue arrow) is the superposition of these dipoles.

This MEI effect can be further extended to nonuniform spin textures, e.g., M skyrmions. According to the aforementioned MEI rule, i.e., the isoperiodic bijection between $\mathbf{P}$ and $\mathbf{S}$, the generated dipoles should also be non-uniform, which form an E-skyrmions, as shown in Figs. 3(b) and 3(c). To verify this expectation, the DFT calculation is performed using a supercell (containing 112 Cr ions) with an M skyrmion in the free layer. Then the E skyrmion of (P_x, P_y, ΔP_z) can be clearly evidenced in the ferromagnetic frozen layer via the DED image, as shown in Fig. 3(d). In this sense, the M skyrmions in one layer can be detected (and even manipulated) in its proximate layer via pure electrical methods.

C. Conditions for magnetoelectric skyrmions

Then the next question is how to stabilize a M skyrmion in one layer while the rest layer keeps ferromagnetic, since the bilayer are "identical" in the chemical component. Luckily, the off-plane polarization from sliding breaks the symmetry between these two layers, opening a route to pursue hetero-magnetism in such a bilayer. So far, the twofold role of sliding ferroelectricity is clear: (i) break the reversal symmetry along

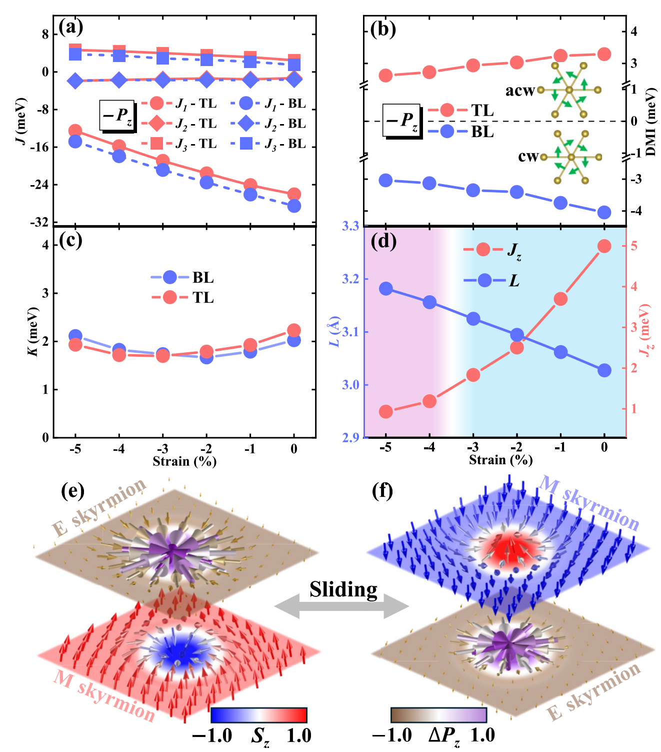

FIG. 4. Layer-resolved magnetic coefficients under biaxial compressive strain and M/E skyrmions. (a) The Heisenberg-type exchange coefficients J_i (i: the first/second/third-nearest-neighbor index). (b) The nearest-neighboring DMI. The signs of DMI of top/bottom layers are opposite, which prefer opposite chirality (clockwise vs counterclockwise). (c) The single-ion magnetocrystalline anisotropy. (d) The interlayer distance L and exchange coefficient (J_z). "TL"/"BL" represents the top/bottom layer, respectively. According to the model simulation, isolated skyrmions can appear in the strained regions [magenta in (d)]. (e), (f) The model simulated spin/dipole textures under −4% strain for $-P_z$ and $+P_z$ states, respectively.

the z axis, which is a precondition to the full MEI function. (ii) create ideal conditions for pursuing hetero-magnetism in homostructures (e.g., CrTeI bilayer).

To demonstrate this effect, the layer-resolved magnetic interactions are calculated as functions of in-plane biaxial strain, as shown in Fig. 4 (see Figs. S8 and S9 in the SM for more details [49]). With increasing compressive strain, the nearest-neighboring ferromagnetic exchange J_1 is significantly suppressed (e.g., ∼50% upon −5% strain) but the DMI (D) is only moderately suppressed (e.g., ∼25% upon −5% strain). Meanwhile, the magnetocrystalline anisotropy K is insensitive to the strain. In this sense, the $|D/J_1|$ ratio becomes larger under compressive strain, which is advantageous to stabilize M skyrmions.

Furthermore, the exchanges are indeed different between two layers, as shown in Fig. 4(a). For the $-P_z$ case, comparing with the bottom layer, J_1 is weaker for $\sim 8 - 15\%$ in the top layer. Meanwhile, the amplitude of D in the top layer is even smaller for $\sim 11 - 19\%$ [Fig. 4(b)]. Thus, the larger $|D/J_1|$ ratio in the bottom layer is in favor of M skyrmions. In addition, the compressive strain enlarges the vdW gap (L) from 3.03 Å to 3.18 Å, which seriously reduces the interlayer exchange J_z by 80% [Fig. 4(d)], which is also advantageous to decouple the magnetic textures between two layers.

By using these coefficients, an atomistic simulation is performed on a spin lattice model [49]. An isolated M skyrmion with diameter ∼4 nm can be indeed obtained in the bottom layer when the compressive strain reaches −4% [Fig. 4(e)]. Meanwhile, an E skyrmion is induced in the ferromagnetic top layer, as a consequence of the aforementioned MEI effect. More interestingly, by sliding one layer to switch to the $+P_z$ state, the roles of top and bottom layers are reversed (see Fig. S10 for J and DMI). Then the M skyrmion can appear in the top layer while the corresponding E skyrmion is generated in the bottom layer [Fig. 4(f)]. The MEI of skyrmion at −4% strain is also confirmed by direct DFT calculations (Fig. S11 in the SM) [49].

More importantly, such MEI effect is robust and general in other vdW (homo)heterostructures as demonstrated in Figs. S12 and S13, and potential challenges related to the stability and practicality are discussed in the SM [49].

IV. CONCLUSION

In summary, a general strategy called magnetoelectric imprint has been proposed, which can map M skyrmions to E skyrmions in the proximate layer via interlayer magnetic couplings and spin-orbit coupling. This kind of E skyrmion is generated via electronic cloud distortion instead of lattice distortions. Furthermore, such a pair of M skyrmion and E skyrmion can be viewed as an emerging quasiparticle (i.e., ME skyrmion), which provides the opportunity for full electrical field characterization of magnetic topological textures.

ACKNOWLEDGMENTS

We are grateful to Haoshen Ye, Ziwen Wang, Dr. Ning Ding, Yu Xing, Xiong Luo, and Dr. Linglong Li for helpful discussions. This work is supported by National Natural Science Foundation of China (Grants No. 12325401, No. 12274069, and No. 124B2064), Natural Science Foundation of Jiangsu Province (Grant No. BK20221451), Postgraduate Research & Practice Innovation Program of Jiangsu Province (Grant No. KYCX24_0362), and SEU Innovation Capability Enhancement Plan for Doctoral Students (Grant No. CXJH_-SEU 25002). Most calculations were done on the Big Data Computing Center of Southeast University.

[1] N. Nagaosa and Y. Tokura, Topological properties and dynamics of magnetic skyrmions, Nat. Nanotechnol. **8**, 899 (2013).

[2] A. Fert, N. Reyren, and V. Cros, Magnetic skyrmions: Advances in physics and potential applications, Nat. Rev. Mater. **2**, 17031 (2017).

[3] S. Mühlbauer, B. Binz, F. Jonietz, C. Pfleiderer, A. Rosch, A. Neubauer, R. Georgii, and P. Böni, Skyrmion lattice in a chiral magnet, Science **323**, 915 (2009).

[4] X. Z. Yu, Y. Onose, N. Kanazawa, J. H. Park, J. H. Han, Y. Matsui, N. Nagaosa, and Y. Tokura, Real-space observation of a two-dimensional skyrmion crystal, Nature (London) **465**, 901 (2010).

[5] Z. Shen, S. Dong, and X. Yao, Manipulation of magnetic topological textures via perpendicular strain and polarization in van der Waals magnetoelectric heterostructures, Phys. Rev. B **108**, L140412 (2023).

[6] X. Yao and S. Dong, Vector vorticity of skyrmionic texture: An internal degree of freedom tunable by magnetic field, Phys. Rev. B **105**, 014444 (2022).

[7] X. Yao, D. Hu, and S. Dong, Modulation of skyrmionic magnetic textures in two-dimensional vdW materials and their heterostructures, iScience **26**, 106311 (2023).

[8] Z. Shen, C. Song, Y. Xue, Z. Wu, J. Wang, and Z. Zhong, Strain-tunable Dzyaloshinskii-Moriya interaction and skyrmions in two-dimensional Janus $Cr_2X_3Y_3$ (X, Y = Cl, Br, I, X ≠ Y) trihalide monolayers, Phys. Rev. B **106**, 094403 (2022).

[9] Y. Tokura and N. Kanazawa, Magnetic skyrmion materials, Chem. Rev. **121**, 2857 (2021).

[10] D. Amoroso, P. Barone, and S. Picozzi, Spontaneous skyrmionic lattice from anisotropic symmetric exchange in a Ni-halide monolayer, Nat. Commun. **11**, 5784 (2020).

[11] H.-M. Zhang, J. Chen, P. Barone, K. Yamauchi, S. Dong, and S. Picozzi, Possible emergence of a skyrmion phase in ferroelectric $GaMo_4S_8$, Phys. Rev. B **99**, 214427 (2019).

[12] N. Romming, C. Hanneken, M. Menzel, J. E. Bickel, B. Wolter, K. von Bergmann, A. Kubetzka, and R. Wiesendanger, Writing and deleting single magnetic skyrmions, Science **341**, 636 (2013).

[13] N. Romming, A. Kubetzka, C. Hanneken, K. von Bergmann, and R. Wiesendanger, Field-dependent size and shape of single magnetic skyrmions, Phys. Rev. Lett. **114**, 177203 (2015).

[14] D. M. Crum, M. Bouhassoune, J. Bouaziz, B. Schweflinghaus, S. Blügel, and S. Lounis, Perpendicular reading of single confined magnetic skyrmions, Nat. Commun. **6**, 8541 (2015).

[15] C. Hanneken, F. Otte, A. Kubetzka, B. Dupé, N. Romming, K. von Bergmann, R. Wiesendanger, and S. Heinze, Electrical detection of magnetic skyrmions by tunnelling noncollinear magnetoresistance, Nat. Nanotechnol. **10**, 1039 (2015).

[16] I. Lima Fernandes, S. Blügel, and S. Lounis, Spin-orbit enabled all-electrical readout of chiral spin-textures, Nat. Commun. **13**, 1576 (2022).

[17] P. Chu, Y. L. Xie, Y. Zhang, J. P. Chen, D. P. Chen, Z. B. Yan, and J. M. Liu, Real-space anisotropic dielectric response in a multiferroic skyrmion lattice, Sci. Rep. **5**, 8318 (2015).

[18] Y. Okamura, F. Kagawa, M. Mochizuki, M. Kubota, S. Seki, S. Ishiwata, M. Kawasaki, Y. Onose, and Y. Tokura, Microwave magnetoelectric effect via skyrmion resonance modes in a helimagnetic multiferroic, Nat. Commun. **4**, 2391 (2013).

[19] M. Mochizuki and S. Seki, Magnetoelectric resonances and predicted microwave diode effect of the skyrmion crystal in a multiferroic chiral-lattice magnet, Phys. Rev. B **87**, 134403 (2013).

[20] X. Yao, J. Chen, and S. Dong, Controlling the helicity of magnetic skyrmions by electrical field in frustrated magnets, New J. Phys. **22**, 083032 (2020).

[21] J. Xia, X. Zhang, X. Liu, Y. Zhou, and M. Ezawa, Universal quantum computation based on nanoscale skyrmion helicity qubits in frustrated magnets, Phys. Rev. Lett. **130**, 106701 (2023).

[22] S. Das, Y. L. Tang, Z. Hong, M. A. P. Gonçalves, M. R. McCarter, C. Klewe, K. X. Nguyen, F. Gómez-Ortiz, P. Shafer, E. Arenholz, V. A. Stoica, S. L. Hsu, B. Wang, C. Ophus, J. F. Liu, C. T. Nelson, S. Saremi, B. Prasad, A. B. Mei, D. G. Schlom *et al.*, Observation of room-temperature polar skyrmions, Nature (London) **568**, 368 (2019).

[23] R. Zhu, Z. Jiang, X. Zhang, X. Zhong, C. Tan, M. Liu, Y. Sun, X. Li, R. Qi, K. Qu, Z. Liu, M. Wu, M. Li, B. Huang, Z. Xu, J. Wang, K. Liu, P. Gao, J. Wang, J. Li *et al.*, Dynamics of polar skyrmion bubbles under electric fields, Phys. Rev. Lett. **129**, 107601 (2022).

[24] S. Yuan, Z. Chen, S. Prokhorenko, Y. Nahas, L. Bellaiche, C. Liu, B. Xu, L. Chen, S. Das, and L. W. Martin, Hexagonal close-packed polar-skyrmion lattice in ultrathin ferroelectric $PbTiO_3$ films, Phys. Rev. Lett. **130**, 226801 (2023).

[25] Y.-T. Shao, S. Das, Z. Hong, R. Xu, S. Chandrika, F. Gómez-Ortiz, P. García-Fernández, L.-Q. Chen, H. Y. Hwang, J. Junquera, L. W. Martin, R. Ramesh, and D. A. Muller, Emergent chirality in a polar meron to skyrmion phase transition, Nat. Commun. **14**, 1355 (2023).

[26] M. R. McCarter, K. T. Kim, V. A. Stoica, S. Das, C. Klewe, E. P. Donoway, D. M. Burn, P. Shafer, F. Rodolakis, M. A. P. Gonçalves, F. Gómez-Ortiz, J. Íñiguez, P. García-Fernández, J. Junquera, S. W. Lovesey, G. van der Laan, S. Y. Park, J. W. Freeland, L. W. Martin, D. R. Lee *et al.*, Structural chirality of polar skyrmions probed by resonant elastic x-ray scattering, Phys. Rev. Lett. **129**, 247601 (2022).

[27] N. Wang, Z. Shen, W. Luo, H.-K. Li, Z.-J. Xu, C. Shi, H.-Y. Ye, S. Dong, and L.-P. Miao, Noncollinear ferroelectric and screw-type antiferroelectric phases in a metal-free hybrid molecular crystal, Nat. Commun. **15**, 10262 (2024).

[28] W. Yang, G. Tian, Y. Zhang, F. Xue, D. Zheng, L. Zhang, Y. Wang, C. Chen, Z. Fan, Z. Hou, D. Chen, J. Gao, M. Zeng, M. Qin, L.-Q. Chen, X. Gao, and J.-M. Liu, Quasi-one-dimensional metallic conduction channels in exotic ferroelectric topological defects, Nat. Commun. **12**, 1306 (2021).

[29] S. Das, Z. Hong, V. A. Stoica, M. A. P. Gonçalves, Y. T. Shao, E. Parsonnet, E. J. Marksz, S. Saremi, M. R. McCarter, A. Reynoso, C. J. Long, A. M. Hagerstrom, D. Meyers, V. Ravi, B. Prasad, H. Zhou, Z. Zhang, H. Wen, F. Gómez-Ortiz, P. García-Fernández *et al.*, Local negative permittivity and topological phase transition in polar skyrmions, Nat. Mater. **20**, 194 (2021).

[30] A. K. Yadav, K. X. Nguyen, Z. Hong, P. García-Fernández, P. Aguado-Puente, C. T. Nelson, S. Das, B. Prasad, D. Kwon, S. Cheema, A. I. Khan, C. Hu, J. Íñiguez, J. Junquera, L.-Q. Chen, D. A. Muller, R. Ramesh, and S. Salahuddin, Spatially resolved steady-state negative capacitance, Nature (London) **565**, 468 (2019).

[31] T. Xu, C. Wu, S. Zheng, Y. Wang, J. Wang, H. Hirakata, T. Kitamura, and T. Shimada, Mechanical rippling for diverse ferroelectric topologies in otherwise nonferroelectric $SrTiO_3$ nanofilms, Phys. Rev. Lett. **132**, 086801 (2024).

[32] S. Picozzi, K. Yamauchi, B. Sanyal, I. A. Sergienko, and E. Dagotto, Dual nature of improper ferroelectricity in a magnetoelectric multiferroic, Phys. Rev. Lett. **99**, 227201 (2007).

[33] J.-J. Zhang, L. Lin, Y. Zhang, M. Wu, B. I. Yakobson, and S. Dong, Type-II multiferroic $Hf_2VC_2F_2$ MXene monolayer with high transition temperature, J. Am. Chem. Soc. **140**, 9768 (2018).

[34] L. Li and M. Wu, Binary compound bilayer and multilayer with vertical polarizations: Two-dimensional ferroelectrics, multiferroics, and nanogenerators, ACS Nano **11**, 6382 (2017).

[35] M. Wu and J. Li, Sliding ferroelectricity in 2D van der Waals materials: Related physics and future opportunities, Proc. Natl. Acad. Sci. USA **118**, e2115703118 (2021).

[36] N. Ding, J. Chen, C. Gui, H. You, X. Yao, and S. Dong, Phase competition and negative piezoelectricity in interlayer-sliding ferroelectric ZrI_2, Phys. Rev. Mater. **5**, 084405 (2021).

[37] G. Kresse and J. Furthmüller, Efficient iterative schemes for *ab initio* total-energy calculations using a plane-wave basis set, Phys. Rev. B **54**, 11169 (1996).

[38] J. P. Perdew, K. Burke, and M. Ernzerhof, Generalized gradient approximation made simple, Phys. Rev. Lett. **77**, 3865 (1996).

[39] Z. Hao, H. Li, S. Zhang, X. Li, G. Lin, X. Luo, Y. Sun, Z. Liu, and Y. Wang, Atomic scale electronic structure of the ferromagnetic semiconductor $Cr_2Ge_2Te_6$, Sci. Bull. **63**, 825 (2018).

[40] M. Pizzochero and O. V. Yazyev, Inducing magnetic phase transitions in monolayer CrI_3 via lattice deformations, J. Phys. Chem. C **124**, 7585 (2020).

[41] A. Togo and I. Tanaka, First principles phonon calculations in materials science, Scr. Mater. **108**, 1 (2015).

[42] A. Togo, F. Oba, and I. Tanaka, First-principles calculations of the ferroelastic transition between rutile-type and $CaCl_2$-type SiO_2 at high pressures, Phys. Rev. B **78**, 134106 (2008).

[43] R. D. King-Smith and D. Vanderbilt, Theory of polarization of crystalline solids, Phys. Rev. B **47**, 1651 (1993).

[44] R. Resta, Macroscopic polarization in crystalline dielectrics: The geometric phase approach, Rev. Mod. Phys. **66**, 899 (1994).

[45] K. Momma and F. Izumi, VESTA 3 for three-dimensional visualization of crystal, volumetric and morphology data, J. Appl. Crystallogr. **44**, 1272 (2011).

[46] L. D. L. Lifshitz and E. M., On the theory of the dispersion of magnetic permeability in ferromagnetic bodies, Phys. Z. Sowjetunion **8**, 51 (1935).

[47] T. Gilbert, Classics in magnetics a phenomenological theory of damping in ferromagnetic materials, IEEE Trans. Magn. **40**, 3443 (2004).

[48] G. P. Müller, M. Hoffmann, C. Dißelkamp, D. Schürhoff, S. Mavros, M. Sallermann, N. S. Kiselev, H. Jónsson, and S. Blügel, Spirit: Multifunctional framework for atomistic spin simulations, Phys. Rev. B **99**, 224414 (2019).

[49] See Supplemental Material at http://link.aps.org/supplemental/10.1103/PhysRevB.111.104422 for calculation details, crystal structure, the calculations of magnetic parameters, the convergence test of k mesh and energy cutoff when calculate the single ion anisotropic coefficient K, and more details about the MEI rules of CrTeI bilayer (nonsliding) and CrTeI/NiI_2 heterostructure, which also contains Refs. [62–64].

[50] I. Dzyaloshinsky, A thermodynamic theory of "weak" ferromagnetism of antiferromagnetics, J. Phys. Chem. Solids **4**, 241 (1958).

[51] T. Moriya, Anisotropic superexchange interaction and weak ferromagnetism, Phys. Rev. **120**, 91 (1960).

[52] A.-Y. Lu, H. Zhu, J. Xiao, C.-P. Chuu, Y. Han, M.-H. Chiu, C.-C. Cheng, C.-W. Yang, K.-H. Wei, Y. Yang, Y. Wang, D. Sokaras, D. Nordlund, P. Yang, D. A. Muller, M.-Y. Chou, X. Zhang, and L.-J. Li, Janus monolayers of transition metal dichalcogenides, Nat. Nanotechnol. **12**, 744 (2017).

[53] J. Zhang, S. Jia, I. Kholmanov, L. Dong, D. Er, W. Chen, H. Guo, Z. Jin, V. B. Shenoy, L. Shi, and J. Lou, Janus monolayer transition-metal dichalcogenides, ACS Nano **11**, 8192 (2017).

[54] J. Heyd, G. E. Scuseria, and M. Ernzerhof, Hybrid functionals based on a screened Coulomb potential, J. Chem. Phys. **118**, 8207 (2003).

[55] J. Heyd, G. E. Scuseria, and M. Ernzerhof, Erratum: "Hybrid functionals based on a screened Coulomb potential" [J. Chem. Phys. 118, 8207 (2003)], J. Chem. Phys. **124**, 219906 (2006).

[56] Z. Fei, W. Zhao, T. A. Palomaki, B. Sun, M. K. Miller, Z. Zhao, J. Yan, X. Xu, and D. H. Cobden, Ferroelectric switching of a two-dimensional metal, Nature (London) **560**, 336 (2018).

[57] Q. Yang, M. Wu, and J. Li, Origin of two-dimensional vertical ferroelectricity in WTe_2 bilayer and multilayer, J. Phys. Chem. Lett. **9**, 7160 (2018).

[58] L. Rogée, L. Wang, Y. Zhang, S. Cai, P. Wang, M. Chhowalla, W. Ji, and S. Lau, Ferroelectricity in untwisted heterobilayers of transition metal dichalcogenides, Science **376**, 973 (2022).

[59] K. Yasuda, X. Wang, K. Watanabe, T. Taniguchi, and P. Jarillo-Herrero, Stacking-engineered ferroelectricity in bilayer boron nitride, Science **372**, 1458 (2021).

[60] M. V. Stern, Y. Waschitz, W. Cao, I. Nevo, K. Watanabe, T. Taniguchi, E. Sela, M. Urbakh, O. Hod, and M. B. Shalom, Interfacial ferroelectricity by van der Waals sliding, Science **372**, 1462 (2021).

[61] C. Huang and E. Kan, Interlayer-spin-interaction-driven sliding ferroelectricity in a van der Waals magnetic heterobilayer, arXiv:2309.07702.

[62] I. A. Sergienko, C. Şen, and E. Dagotto, Ferroelectricity in the magnetic E-phase of orthorhombic perovskites, Phys. Rev. Lett. **97**, 227204 (2006).

[63] H. Katsura, N. Nagaosa, and A. V. Balatsky, Spin current and magnetoelectric effect in noncollinear magnets, Phys. Rev. Lett. **95**, 057205 (2005).

[64] J. Liang, W. Wang, H. Du, A. Hallal, K. Garcia, M. Chshiev, A. Fert, and H. Yang, Very large dzyaloshinskii-moriya interaction in two-dimensional janus manganese dichalcogenides and its application to realize skyrmion states, Phys. Rev. B **101**, 184401 (2020).